Modeling primary production from carbon flux and satellite data

Mikhail Sokolov

Southern Federal University, 105/42 Bolshaya Sadovaya Str., Rostov-on-Don, 344006, Russia
Correspondence: mikhail39sokolov@tuta.io

Abstract

Gross Primary Production (GPP) is an important metric for tracking vegetation health on a large scale and plays a vital role in the Earth's carbon cycle. Understanding the daily fluctuations in GPP is key for grasping how plants respond to environmental stress, which are likely to occur more frequently due to climate change. With advanced satellites, we can now gather surface data like solar radiation and land surface temperature more frequently, potentially helping us to estimate GPP daily.

1. Introduction

Terrestrial gross primary production (GPP) is one of the largest CO_2 fluxes between land and atmosphere, which is a key component in understanding the global carbon cycle and carbon-climate feedbacks (Running et al., 2000; Janzen, 2004; Beer et al., 2010; Xia et al., 2015). The impact of human-driven climate change on terrestrial GPP affects the heat, water, and carbon budgets over terrestrial surfaces, further complicating the projection of climate change (Ozanne et al., 2003; Cox et al., 2013; Friedlingstein et al., 2019). On the other hand, GPP is a key indicator for understanding vegetation productivities at the regional scale (Kalfas et al., 2011; Peng et al., 2019; Jiang et al., 2021; Li et al., 2021a). Changes in GPP due to extreme events, such as heat waves, droughts, and heavy rainfall, are linked to impacts on crop productivity and regional-scale ecosystems (Ciais et al., 2005; Reeves et al., 2005; Zscheischler et al., 2014; Chen et al., 2019; Xu et al., 2020). Extreme events are projected to occur more intensely and frequently with climate change (Imada et al., 2018; Zhang et al., 2022). Thus, understanding and monitoring GPP at various spatiotemporal scales are important for addressing impact of climate change.

Satellite remote sensing represents a widely employed methodology for estimating GPP at regional to global scales over 8-day or longer temporal scales. Its repeated and expansive coverage of observation enables the monitoring of spatiotemporal variations in terrestrial GPP. To date, Many GPP estimation models have been proposed using remote sensing data, including data-driven models (Yang et al. 2007; Jung et al. 2011), semi-empirical models (Goets et al. 1999; Heinsch et al. 2006; Yuan et al. 2007), and process-based models (Sasai et al. 2005). These models have been widely applied to monitor seasonal and interannual variations in GPP (Goetz et al. 2000; Running et al., 2004). Such approaches

are effective to understand terrestrial GPP variations in an effective way, because the model algorithms are much faster and simplified compared to process-based modeling and can obtain better performance in an effective manner (Cai and Prentice, 2019).

With an advancements of new generation geostationary satellites, such as Himawari-8, Geostationary Operational Environmental Satellite R-Series (GOES-R), Geostationary Korea Multi-Purpose Satellite-2A (GEO-KOMPSAT-2A), and FengYun-4A, possibility to monitor sub-daily GPP is increasing (e.g., Bessho et al., 2016; Wang et al., 2020). The optical sensors on these satellites have been added multiple solar reflective and thermal infrared bands and improved spatiotemporal resolution, enabling them to provide land surface parameters such as downwelling shortwave radiation (SR_d), vegetation indices, and land surface temperature (LST) that are useful for estimating sub-daily GPP (Cheng et al., 2020; Chen et al., 2021). Xiao et al. (2021) demonstrated that a semi-empirical light use efficiency (LUE) model driven by the Himawari-8 data has a possibility to represent the variation in diurnal GPP due to a heatwave at one site in Australia. Khan et al. (2022) attempted to monitor GPP in an oak savanna in California, USA, using different semi-empirical models driven by GOES-R data. Of those models, an LUE model and a light response curve-product of near-infrared reflectance of vegetation and photosynthetically active radiation (LRC-NIRvP) model were shown to capture a shift in peak GPP to the morning, a unique diurnal pattern in the dry summer. Jeong et al (2023) showed that atmospheric corrected and Bi-directional Reflectance Distribution Function (BRDF) normalized NIRvP tracks diurnal GPP well at cropland and forest sites in South Korea.

There are still issues regarding the applicability of semi-empirical models driven by geostationary satellite data to diurnal GPP estimation. Previous studies have applied models focusing on semi-arid regions (Xiao et al., 2021; Khan et al., 2022), however, further discussion of their applicability under humid regions is also necessary. The models are required to represent GPP variability induced by a large diurnal range of irradiance, which were not assumed originally. Furthermore, the models also need to represent the difference in photosynthetic rate between clear and cloudy conditions (Alton et al., 2007; Zhang et al., 2020), which changes dramatically under humid climates. Besides, it is necessary to clarify not only the issues regarding the model itself, but also the effects caused by the input data uncertainties when performing a regional estimation.

To address the above issues, this study aimed to evaluate the effectiveness of the LUE models in estimating diurnal GPP at cropland and forest sites in East Asia. In order to improve the bias of existing LUE models in diurnal estimation, we propose a refined model that considers large diurnal ranges of irradiance by controlling LRC. We also run the refined LUE model using Himawari-8 SR_d data and numerical weather model data as inputs, and

discussed the issues in regional GPP estimation. Additionally, we utilized Himawari-8 LST data to represent the thermal environment at vegetation surfaces, and discussed its effectiveness in estimating environmental stress.

2. Materials and methods

2.1. Materials

2.1.1. In-situ flux tower data

Calibration and verification of the LUE models were performed using flux tower observation data at four vegetation sites: Takayama deciduous broadleaf forest site (TKY); Cheorwon rice paddy site (CRK); Gwangneung coniferous forest site (GCK); and Gwangneung deciduous forest site (GDK). The sites' locations in the Japanese archipelago and the Korean peninsula are shown in Figure 1, and their geographic conditions are shown in Table 1. The climate around TKY site in the highlands is warm-summer humid continental climate (Dfb) of the Köppen climate classification, whereas CRK, GCK, and GDK sites are monsoon-influenced hot-summer humid continental climate (Dwa). All these sites are registered in the AsiaFlux network (https://www.asiaflux.net/).

Table 1. Site information used in this study.

Site name	Takayama deciduous broadleaf forest	Cheorwon rice paddy	Gwangreung coniferous forest	Gwangreung deciduous forest
Site code	TKY	CRK	GCK	GDK
Location	36.146 °N 137.423 °E	38.201 °N 127.251 °E	37.748 °N 127.162 °E	37.749 °N 127.149 °E
Altitude	1420 m	181 m	132 m	252 m
Vegetation type	Cool temperate deciduous forest	Rice paddy	Coniferous forest	Mixed deciduous forest
Canopy height	15–20 m	~1 m	28 m	20 m
Sensor (SR_d, LR_u, LR_d)	MR-50, EKO Co., Japan	CNR4, Kipp & Zonen B.V., Netherlands	CNR1, Kipp & Zonen B.V., Netherlands	CNR1, Kipp & Zonen B.V., Netherlands
Sensor (CO_2, LE, H)				
- 3D sonic anemometer	DA600-3TV, KAIJO Co., Japan	CSAT3, Campbell Sci., Inc., USA	CSAT3, Campbell Sci., Inc., USA	CSAT3, Campbell Sci., Inc., USA
- Infrared gas analyzer	LI-6262, LI-COR Inc., USA	LI-7200, LI-COR Inc., USA	LI-7200, LI-COR Inc., USA	EC155, Campbell Sci., Inc., USA

Mounting height	25 m	10 m	40 m	38 m

The flux and meteorological variables used were GPP, SR_d, up- and downwelling longwave radiation (LR_u and LR_d, respectively), air-temperature (T_a), and relative humidity (RH). These variables were observed at the height above the canopy and were provided every 30 min. The information on the instruments and their mounting heights at each site are listed in Table 1. We used observations when SR_d was greater than 0 Wm^{-2} for the period June 1–August 31, 2016–2018. LR_u and LR_d were used to estimate LST, and T_a and RH were used to estimate vapor pressure deficit (VPD). The estimation of LST is based on thermal radiative transfer theory (e.g., Wang et al., 2008; Malakar et al., 2018; Duan et al., 2021), thus requiring the surface 3–14 μm broadband emissivity (BBE) as well as longwave radiation. The BBE at each site was estimated from the ASTER Global Emissivity Database (Hulley et al., 2015) at 100 m resolution using the conversion formula proposed by Cheng et al. (2013).

2.1.2. AHI data

Himawari-8 AHI SR_d and LST data from June 1 to August 31, 2016–2018 were used for the regional estimation of the GPP covering the area around the Japanese archipelago and the Korean peninsula. The SR_d and LST data were obtained from the Center for Environmental Remote Sensing (CEReS) at Chiba University, Japan. These data are geometrically corrected and resampled to an equal latitude-longitude grid. The spatial resolutions of the SR_d and LST data are 0.01° and 0.02°, respectively, and the temporal resolutions are both 10 min. The AHI SR_d estimation is based on radiative transfer calculations using a neural network. Cloud optical thickness, cloud-particle effective radius, and surface albedo are estimated from the AHI observations and act as the primary inputs driving the high spatiotemporal variability of SR_d. A homogeneous plane-parallel and single-layer cloud model (Nakajima and Nakajima, 1995; Kawamoto et al., 2001) are assumed in the retrieval of cloud optical thickness and cloud-particle effective radius. The AHI SR_d has shown an accuracy of approximately 70–80 Wm^{-2} root mean square error (RMSE) under all-sky conditions in validation using ground observations (Damiani et al., 2018). The AHI LST is retrieved using a nonlinear three band method, which requires brightness temperature and land surface emissivity (LSE) of AHI three thermal infrared (TIR) bands (centered at 10.4, 11.2, and 12.4 μm) as the primary inputs. The LSE of the three TIR bands were estimated by a semi-empirical method based on land cover classifications and Normalized Difference Vegetation Index (NDVI). Uncertainty of the AHI LST is less than 2.0 °C for a fully vegetated pixel.

2.1.3. MODIS product

The fraction of photosynthetically active radiation (FPAR), an input of LUE models was obtained from MODIS combined Leaf Area Index (LAI) and FPAR product (MOD15A2H Collection 6.1: Myneni et al., 2002; Yan et al., 2016). The product is generated as 8-day composite at 500 m resolution, and we used the FPAR data from June 1 to August 31, 2016–2018. The FPAR data were processed for quality control and gap-filling. Diurnal changes in FPAR were not considered and it was assumed to change at 8-day intervals. LAI and FPAR are estimated by an algorithm based on look-up tables (LUTs), using MODIS surface reflectance at 7 spectral bands as primary inputs. The LUT is generated from a three-dimensional radiative transfer model that considers the optical properties of leaves, stems, and soil in the vegetation canopy and links the surface spectral bi-directional reflectance factors to both the structural and optical properties of the vegetation canopy and soil. The LUTs include six biome types, and the biome types are classified from MODIS land cover data.

2.1.4. Numerical model data

The Ta and RH data from June 1 to August 31, 2016–2018 used for the regional estimation of the GPP were obtained from the AMATERASS dataset, the same source of the AHI SR_d (http://www.amaterass.org/data.html). To begin with, the T_a and RH data are the analysis data of the meso-scale model of the Japan Meteorological Agency (JMA-MSM; Saito et al., 2006) which is a numerical weather prediction model. The spatial resolution is 5 km, and the temporal resolution is 3 hours (00, 03, 06, 09, 12, 15, 18, and 21 coordinated universal time (UTC)). In the AMATERASS data set, these spatiotemporal resolutions are interpolated to the 0.01° and 10-min resolutions, similar to the AHI SR_d.

2.2. Model description

LUE models have been widely used in satellite based GPP estimation (e.g., Heinsch et al., 2006; Chen et al., 2009; Yuan et al., 2010; Cai and Prentice, 2019). The LUE model is based on the assumption that GPP can be directly expressed using absorbed photosynthetically active radiation (APAR) and LUE, defined as the efficiency of producing carbon from APAR (Monteith, 1972). The LUE is assumed to decrease from the theoretical potential value by factors of environmental stresses due to temperature and dryness near the vegetation canopy surface. The general form of the LUE model can be written as:

$$GPP = PAR \times FPAR \times LUE_{max} \times f\left(T_s, W_s, \ldots\right) \quad (1)$$

where PAR is photosynthetically active radiation ($Jm^{-2}s^{-1}$), FPAR is fraction of absorbed PAR, LUE_{max} is the potential LUE (gCJ^{-1}) under ideal environmental conditions, and f(T_s, W_s, ...) is a factor of environmental stress including temperature stress (T_s) and water stress

(W_s). The product of PAR and FPAR is the APAR, and the product of LUE_{max} and f is the actual LUE. PAR was estimated as $SR_d \times 0.5$ (McCree et al., 1981).

In this study, we used MODIS GPP model, eddy covariance (EC)-LUE model, and our proposed refined LUE models for estimating the diurnal changes in GPP. The MODIS GPP and EC-LUE models have been widely used for GPP estimation in various ecosystems (Yuan et al., 2014; Yuan et al., 2019; Jiang et al., 2021; Li et al., 2021b; Khan et al., 2022), and they each have different calculation of environmental stress factor. Corresponding to the different magnitudes of environmental stress factors, the magnitude of LUE_{max} also differs between the models.

2.2.1. MODIS GPP model

The MODIS GPP model (Running et al., 2004) is an LUE model used in the MODIS GPP product (MOD17), and f in eq. (1) is calculated as follows:

$$f = T_s \times W_s \tag{2}$$

$$T_s = ¿ \tag{3}$$

$$W_s = \begin{cases} 0 \wedge VPD_{max} \leq VPD \\ \dfrac{VPD_{max} - VPD}{VPD_{max} - VPD_{min}} \; VPD_{min} < VPD < VPD_{max} \\ 1 \wedge VPD \leq VPD_{min} \end{cases} \tag{4}$$

where T_{min} (°C) is the air temperature at which LUE is 0 due to low-temperature stress, T_{max} (°C) is the air temperature at which LUE is 1 under ideal VPD, VPD_{min} (hPa) is the VPD at which LUE is 1 under ideal T_a, and VPD_{max} (hPa) is the VPD at which LUE is 0 due to water stress. T_a (°C) and VPD (hPa) are observed values. Default values for these parameters are assigned to each land cover classification (Running et al., 2000; Mu et al., 2007), as shown in Table 2. Since the MODIS GPP model has originally been used to estimate GPP longer than daily scale, T_a represents the daily minimum temperature, and T_{min} and T_{max} are the corresponding values. In this study, however, T_a was used as T_a every 30 min within a day (Khan et al., 2022).

2.2.2. EC-LUE model

The EC-LUE model developed by Yuan et al. (2007) calculates f in eq. (1) as follows:

$$f = min\left(T_s, W_s\right) \tag{5}$$

$$T_s = \begin{cases} 0 \wedge T_a < T_{min} \vee T_{max} < T_a \\ \dfrac{(T_a - T_{min})(T_a - T_{max})}{(T_a - T_{min})(T_a - T_{max}) - (T_a - T_{opt})^2} \wedge T_{min} \le T_a \le T_{max} \end{cases} \quad (6)$$

$$W_s = \frac{VPD_0}{VPD + VPD_0} \quad (7)$$

where T_{opt} (°C) is the optimal air-temperature for photosynthesis (LUE is 1 under ideal VPD), T_{min} and T_{max} are the air-temperatures at which LUE is 0 due to low- and high-temperature stress, respectively, and VPD_0 is the VPD at which W_s is 0.5. The EC-LUE model considers temperature stress due to high temperatures as well as low temperatures, whereas the MODIS-GPP model does not consider stress due to high temperatures. Default values for the parameters are assigned to each land cover classification (Yuan et al., 2019), as shown in Table 2. The f is taken to be the minimum value in T_s and W_s following Liebig's Law.

Table 2. Default values of LUE model parameters for each site. The parameters are assigned by land cover classification. The land cover classes corresponding to the sites were referred to the MCD12Q1 Collection 6 product (Sulla-Menashe et al., 2019). The GCK, GDK, CRK, and TKY sites are mixed forest, deciduous broadleaf forest, cropland, and mixed forest, respectively.

LUE model	Parameter	GCK	GDK	CRK	TKY
MODIS GPP	T_{min} (℃)	-7.00	-6.00	-8.00	-7.00
	T_{max} (℃)	9.50	9.94	12.02	9.50
	VPD_{min} (hPa)	6.5	6.5	6.5	6.5
	VPD_{max} (hPa)	24.0	16.5	43.0	24.0
	LUE_{max} (gC·MJ^{-1})	1.051	1.165	1.044	1.051
EC-LUE	T_{min} (℃)	0.00	0.00	0.00	0.00
	T_{opt} (℃)	20.33	20.33	20.33	20.33
	T_{max} (℃)	40.00	40.00	40.00	40.00
	VPD_0 (hPa)	4.1	5.4	8.9	4.1
	LUE_{max} (gC·MJ^{-1})	3.46	2.02	2.85	3.46

2.2.3. Refined LUE models

We proposed a refined LUE model in which the APAR is scaled by the light-response curve based on the Michaelis-Menten model (Michaelis and Menten, 1913). The Michaelis-Menten model expresses a relationship between APAR (or PAR) and GPP as a rectangular hyperbolic light-response curve by considering the photochemical efficiency of

photosynthesis at low irradiance and light saturation at extremely high irradiance. In estimating diurnal GPP, low irradiance during twilight and light saturation around noon should be assumed. Thus, the term for APAR (= PAR × FPAR) in eq. (1) is scaled as $APAR_{LRC}$ by the light response curves as follows:

$$APAR_{LRC} = \frac{\alpha APAR \beta}{\beta + \alpha APAR} \quad (8)$$

where α is the initial slope of the light–response curve and β is the maximum APAR at the light saturation point. The $APAR_{LRC}$ increases initially with PAR. Its increasing trend levels off as PAR exceeds the light saturation point and eventually becomes β. The refined MODIS GPP and EC-LUE models are referred to as the LRC-MODIS model and the LRC-ECLUE model, respectively.

2.3. Analysis

2.3.1. Calibration and verification of LUE models

Four LUE models were calibrated for each site using flux tower observation data. The parameters calibrated were T_{max}, VPD_{max}, and LUE_{max} for the MODIS GPP model; T_{opt}, VPD_0, and LUE_{max} for the EC-LUE model; α, β, T_{max}, VPD_{max}, and LUE_{max} for the LRC-MODIS model; and α, β, T_{opt}, VPD_0, and LUE_{max} for the LRC-ECLUE model. The remaining parameters, such as T_{min} and VPD_{min} for the MODIS GPP model and T_{min} and T_{max} for the EC-LUE model, were used as default values shown in Table 2. This is because the covariance among parameters in relation to GPP becomes large if all parameters are optimized simultaneously without any constraints (Yang et al., 2007). Differential evolution, a global optimization method, was applied to the calibration. The observation data for the entire period at each site were randomly split, with 70% as calibration data and 30% as verification data.

The verification accuracies of the four LUE models were compared using the linear regression analysis, coefficient of determination (R^2), root mean square error (RMSE), mean absolute error (MAE), and normalized MAE (NMAE) between GPP observations and estimates as the evaluation indices. The LUE models tend to have larger estimation errors on extremely hot days or cloudy days (Zhang et al., 2020; Khan et al., 2022). We thus examined the error tendencies of each LUE model in estimating the diurnal GPP on extremely hot and cloudy days. The extremely hot days were defined as the five days with the highest daily maximum T_a during the analysis period. For cloudy days, cases with a clearness index (CI) < 0.3 were extracted. The CI is expressed as follows (Gu et al., 1999; Boland et al., 2008; Yang et al., 2019).

$$CI = \frac{SR_d}{SR_e} \quad (9)$$

where SR_e is the extraterrestrial solar radiation ($Jm^{-2}s^{-1}$). The calculation of SR_e was followed by Allen et al. (2006).

2.3.2. GPP estimation using AHI data

GPP estimation using AHI SR_d data as input was performed using the LUE model, which had the best generalization performance in the verification using flux tower observation data. Other inputs for FPAR, T_a and VPD were the MODIS FPAR data and MSM T_a and VPD data, which are available for the regional estimation. The LRC-ECLUE model was applied as the best model, as described in detail below in section 3.2. The LUE model parameters were values calibrated with flux tower observation data. In addition to the estimation accuracy of GPP under all-sky conditions, the accuracies under clear- and cloudy-sky conditions were also investigated, taking into account the error characteristics of the input data varying with cloud cover. The clear- and cloudy- conditions were distinguished based on the cloud masks included in the AHI LST data.

Furthermore, GPP estimation by using LST instead of T_a in T_s estimation was attempted, and the applicability of the AHI LST was investigated. The LST reflects the heat and water budgets of the vegetation surface and near-surface meteorological conditions (Farella et al., 2022). Moreover, the AHI LST has a higher spatiotemporal resolution (~ 2 km and 10 min) than numerical model T_a and VPD (several ~ 100 km grid and several hourly intervals). Therefore, the AHI LST have a potential to detect diurnal environmental stress more precisely in wide-area estimations. The LUE model using LST was calibrated with T_{max} set to 50 °C because LST could be ~10 °C higher than the T_a during the day. The calibration was also performed using in-situ data.

3. Results

3.1. Calibration

The MODIS GPP and EC-LUE models with default parameters showed underestimation in most cases (gray dots in Figure 1a–g). Furthermore, the difference between the estimated and tower GPPs tended to increase as the tower GPP increased. These underestimation tendencies were weakest at the CRK site and strongest at the GDK site. At the GDK site, most estimates were < 0.4 $gC \cdot m^{2} \cdot 30\text{-}min^{-1}$ for both models, although the tower GPPs could be > 0.8 $gC \cdot m^{-2} \cdot 30\text{-}min^{-1}$ (Figure 1b and 2f). The MODIS GPP model showed smaller linear

regression slopes indicating a greater underestimation tendency than the EC-LUE model. GCK and TKY sites are assigned to the same biome type and have the same default values for model parameters (Table 2). However, the EC-LUE model overestimated at TKY sites and underestimated at GCK sites (Figure 1e and 2h).

Calibration improved underestimation in almost all cases, and improved overestimation only for the EC-LUE model at TKY site (Figure 1). The MODIS GPP model showed large changes in all three parameters from their default values, whereas the EC-LUE model showed changes mainly in T_{opt} and VPD_0, the parameters related to stress (Tables 3 and 4). Model parameter differences among sites after the calibration mostly retained their relationships from the default values. For example, the CRK site in the cropland class had higher default values for T_{max}, VPD_{max}, and VPD_0 than other sites, and the characteristics were still shown after the calibration. The default values of the parameters for the GCK and GDK sites were close, and the calibrated parameters for both sites also did not show substantial differences. However, the calibration results for the GCK and TKY sites differed substantially from each other, even though they were in the same land cover class. The LRC-MODIS and LRC-ECLUE models had higher LUE_{max} and lower stresses (e.g., higher VPD_{max} and VPD_0) than the original models since the APAR was controlled by the LRC.

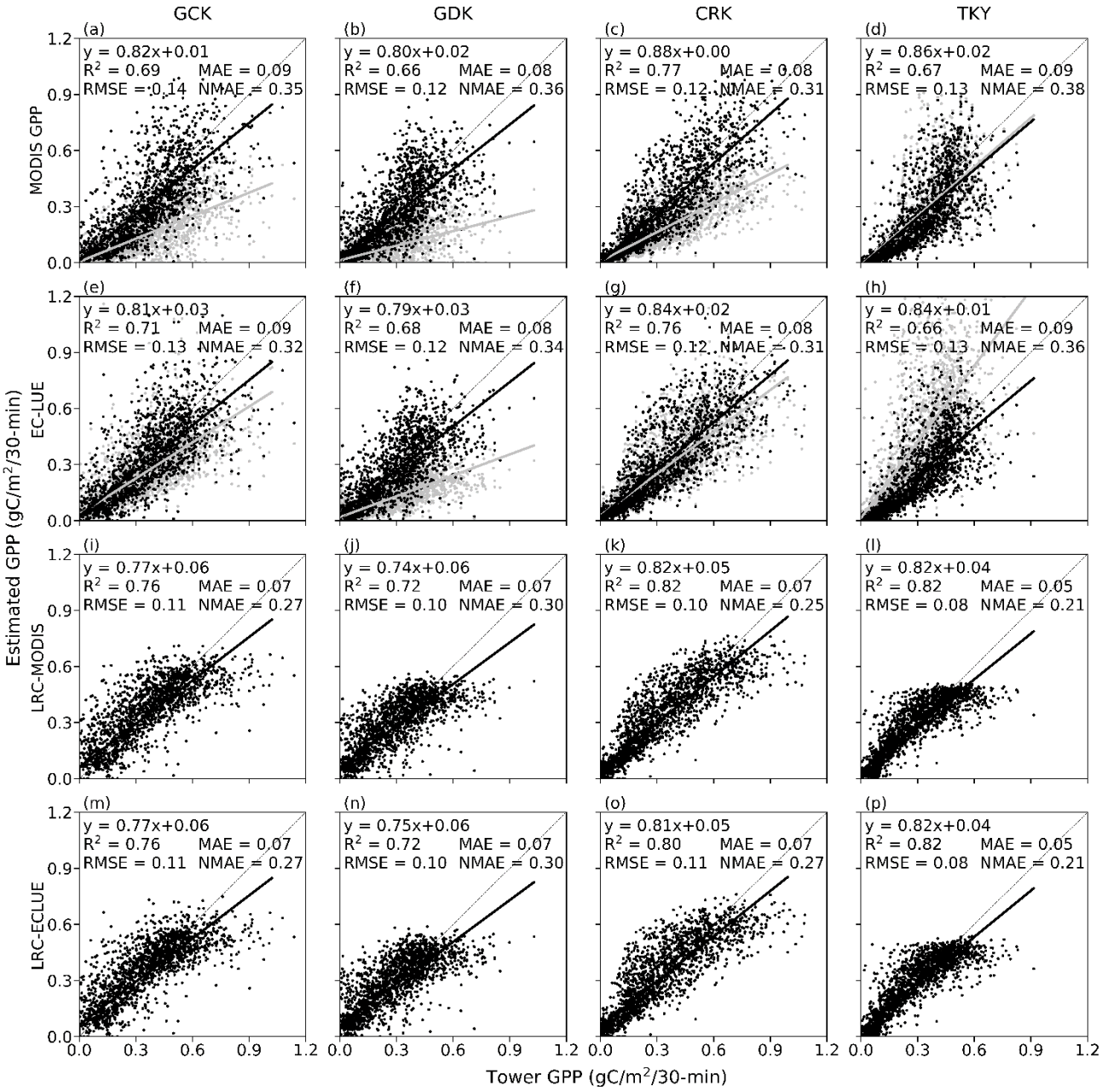

Figure 1. Scatter plots for verification results of (a–d) MODIS GPP model, (e–h) EC-LUE model, (i–l) LRC-MODIS, and (m–p) LRC-ECLUE model. Gray dots show the estimated GPP using default values of the LUE model parameters and black dots show the estimated GPP using calibrated petameters.

Table 3. Calibrated LUE model parameters using flux tower observation data.

LUE model	Parameter	GCK	GDK	CRK	TKY
MODIS	T_{max} (℃)	13.8	14.2	39.9	17.9
	VPD_{max} (hPa)	39.9	38.3	39.8	27.3
	LUE_{max} ($gC \cdot MJ^{-1}$)	1.51	1.72	2.40	1.03

EC-LUE	T_{opt} (℃)	12.3	11.8	20.7	23.3
	VPD_0 (hPa)	8.0	8.7	20.9	9.7
	LUE_{max} ($gC \cdot MJ^{-1}$)	2.92	3.17	2.21	1.48
LRC-MODIS	T_{max} (℃)	13.24	10.22	38.52	17.29
	VPD_{max} (hPa)	50.0	52.8	48.5	52.5
	LUE_{max} ($gC \cdot MJ^{-1}$)	6.62	6.09	9.85	3.99
	α	0.54	0.58	0.50	1.02
	β	86.7	82.3	88.2	85.3
LRC-ECLUE	T_{opt} (℃)	19.0	17.1	39.7	24.2
	VPD_0 (hPa)	28.1	34.5	25.6	39.4
	LUE_{max} ($gC \cdot MJ^{-1}$)	8.03	7.10	8.58	6.06
	α	0.51	0.58	0.61	0.73
	β	89.2	85.1	98.6	63.9

3.2. Verification results and tendencies in diurnal GPP estimation

The LRC-MODIS and LRC-ECLUE models showed higher R^2 and lower RMSE, MAE, and NMAE than the original models (Figure 1). The R^2 increased from 0.66–0.77 to 0.72–0.82, RMSE decreased from 0.12–0.14 to 0.08–0.11 ($gC \cdot m^{-2} \cdot 30\text{-}min^{-1}$), and NMAE decreased from 0.31–0.38 to 0.21–0.30. The MODIS GPP and EC-LUE models showed similar evaluation scores, as did the relationship between LRC-MODIS and LRC-ECLUE models. The scatter plots for the original LUE models showed a nonlinear relationship, with underestimation at low GPP and overestimation at high GPP (Figure 1 a–h). The LRC-MODIS and LRC-ECLUE models showed roughly linear distribution patterns in the scatter plots (Figure 2 i–p), although the linear regression slopes (0.74–0.82) were smaller than those of the original models (0.79–0.88).

For the extremely hot days, the original models showed tendencies to overestimate around noon and underestimate at evening (Figure 2). The MODIS GPP model showed these trends more intensely than the EC-LUE model, especially overestimation around noon at the CRK and TKY sites and underestimation around evening at the GCK, GDK, and TKY sites. These tendencies of the original models are also consistent with the nonlinear distribution patterns (i.e., overestimation at high GPP and underestimation at low GPP) shown in Figure 1a–h. On the other hand, the LRC-MODIS and LRC-ECLUE models improved these tendencies. Moreover, both the LRC-MODIS and LRC-ECLUE models showed earlier timing of the diurnal GPP peak than the original models at all sites, and the timing were closer to those of the observational peak at the GCK, GDK, and TKY sites.

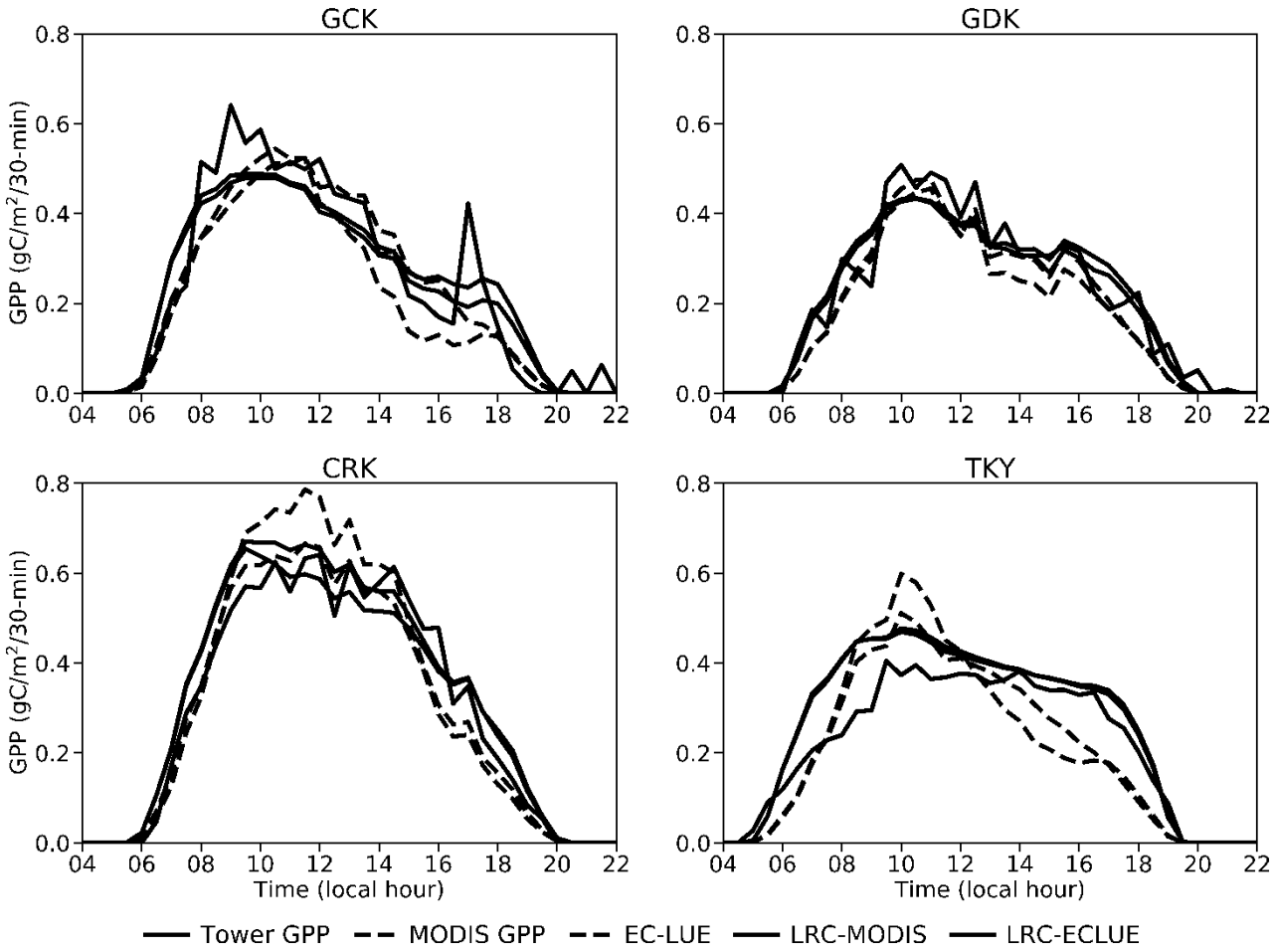

Figure 2. Mean diurnal changes in GPP for the five days with the highest daily maximum T_a for the entire period at each site. The solid black and gray shaded regions show the mean value and ±1 standard deviation of the tower observations, respectively. The blue dashed, red dashed, blue solid, and red solid lines show the mean estimates of the MODIS GPP, EC-LUE, LRC-MODIS, and LRC-ECLUE models, respectively.

For the cloudy days, the original models tended to underestimate throughout the day, with the difference from the tower GPPs increasing especially around the noon (Figure 3). This is consistent with the underestimation at low GPP shown in Figure 1. The underestimations were especially noted at the CRK and TKY sites, with estimated GPPs being smaller than the tower GPPs by > 0.1 $gC \cdot m^{-2} \cdot 30\text{-}min^{-1}$ around noon (Figure 3). The LRC-MODIS and LRC-ECLUE models improved these underestimations. The improvements in estimation accuracy were noticeable compared to those on extremely hot days. The timing of the diurnal GPP peak did not differ between the LRC- and the original models, unlike in the cases of the extremely hot days.

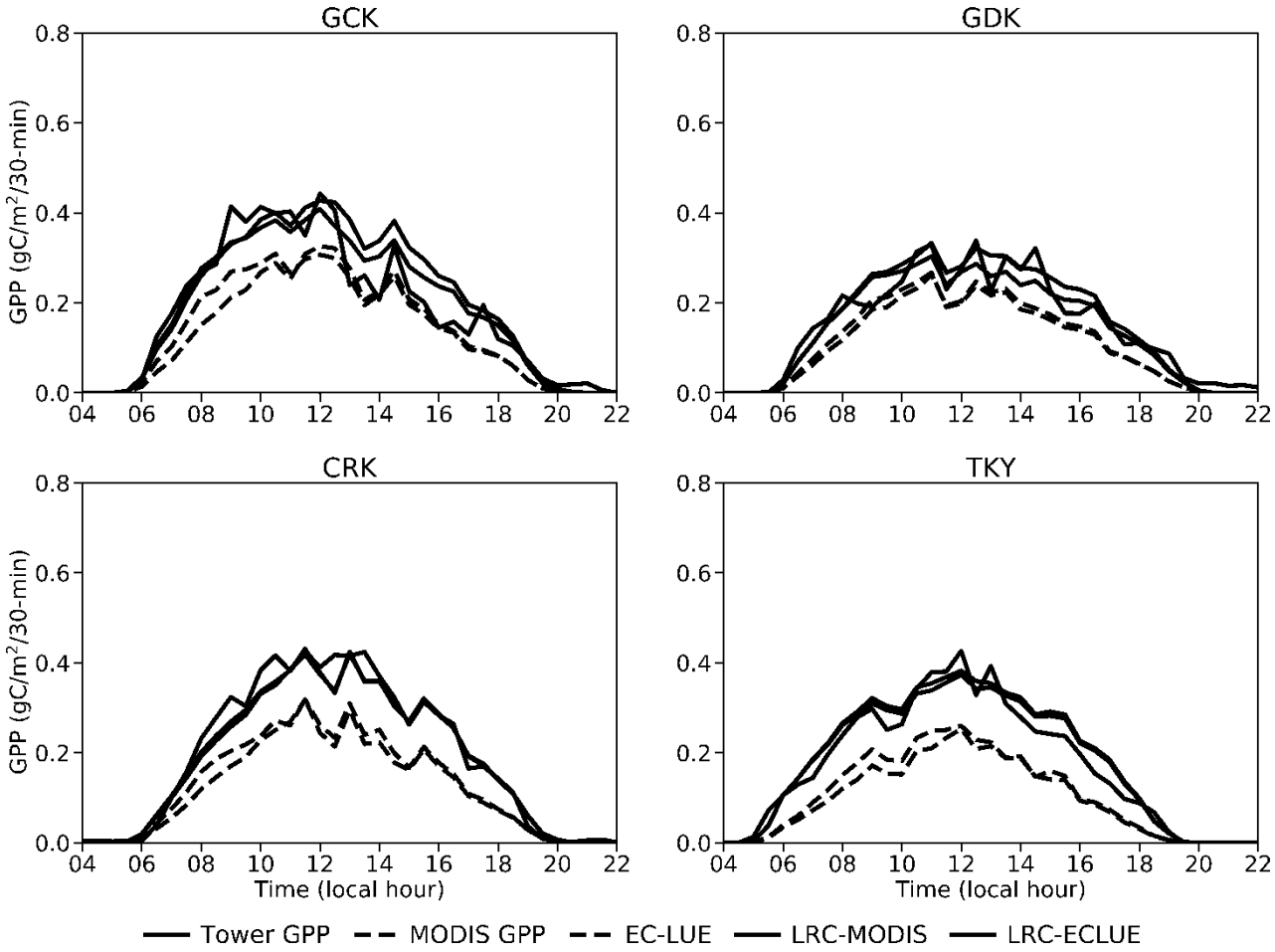

Figure 3. Mean diurnal changes in GPP for cloudy days with the clearness index < 0.3 at each site. The solid black and gray shaded regions show the mean value and ±1 standard deviation of the tower observations, respectively. The blue dashed, red dashed, blue solid, and red solid lines show the mean estimates of the MODIS GPP, EC-LUE, LRC-MODIS, and LRC-ECLUE models, respectively.

3.3. GPP estimation using AHI data

The LRC-ECLUE model using AHI and MSM data as input showed accuracy comparable to the verification results under both clear- and cloudy-sky conditions (Figures 1, 5e, and 6d). The estimation accuracy under clear-sky conditions was 0.12 for RMSE, 0.09 for MAE, and 0.29 for NMAE (Figure 5e), whereas verification results showed 0.08–0.11 for RMSE, 0.05–0.07 for MAE, and 0.21–0.30 for NMAE (Figure 1i–l). The linear regression slope and R^2 under clear sky conditions (0.68 and 0.68, respectively), however, were smaller than those of the verification results (0.74–0.82 and 0.72–0.82, respectively). On the other hand, the cloudy conditions showed better linear regression slope, R^2, RMSE, and MAE (0.73, 0.72, 0.10, and 0.07, respectively) than those under the clear-sky conditions (Figures 5e and 6d).

However, the NMAE was higher under cloudy conditions because GPP was generally lower than under clear-sky conditions. AHI and MSM data were overestimated and underestimated relative to in-situ data, which affected GPP estimation. The AHI PAR, the main factor determining the magnitude of GPP estimates, showed a positive bias of 18.4 $W \cdot m^{-2}$ and 13.3 $W \cdot m^{-2}$ for clear-sky and cloudy conditions, respectively (Figures 5a and 6a). This positive bias caused overestimation in many cases of GPP estimation, as shown in Figures 5e and 6d. Cases with extremely high PAR were suppressed by the LRC (Eq. 8), which conversely caused underestimation in GPP estimation. For inputs regarding environmental stress, MSM VPD showed a positive bias in both clear-sky and cloudy conditions (Figures 5b and 6b), whereas MSM T_a showed a negative bias in the high temperature range (> 20 ℃) in clear-sky conditions and a positive bias in the low temperature range (< 20 ℃) in cloudy conditions (Figures 5c and 6c). These MSM VPD and T_a biases caused underestimation of W_s and overestimation of T_s, respectively, from Eqs. 6 and 7. GPP estimated using AHI LST (LST-based GPP) showed almost identical RMSE, MAE, and NMAE as the GPP estimated using T_a (T_a-based GPP) (Figure 5f). The calibrated parameters of LST-based GPP also showed similar magnitudes to those of the T_a-based GPP (Tables 3 and 4). The AHI LSTs showed a positive bias at high temperatures, causing underestimates of T_s and GPP. Consistent with this, the regression slope in comparison to in-situ GPP (0.68) was smaller than that of T_a-based GPP (0.74) (Figure 5f). LST-based GPP tended to overestimate environmental stress under extreme high temperature conditions (Figure 6). In the mixed forest during the heat wave shown in Figure 7, LST exceeded 40 °C while T_a reached 35 °C during daytime. In addition, the peak in the diurnal changes of LST was about 2–3 hours earlier than that of T_a. The LST-based GPP showed a sudden depression during daytime corresponding to the extreme high LST and its timing. During the periods when the difference between LST and T_a was small, the GPP estimates of the two were almost identical.

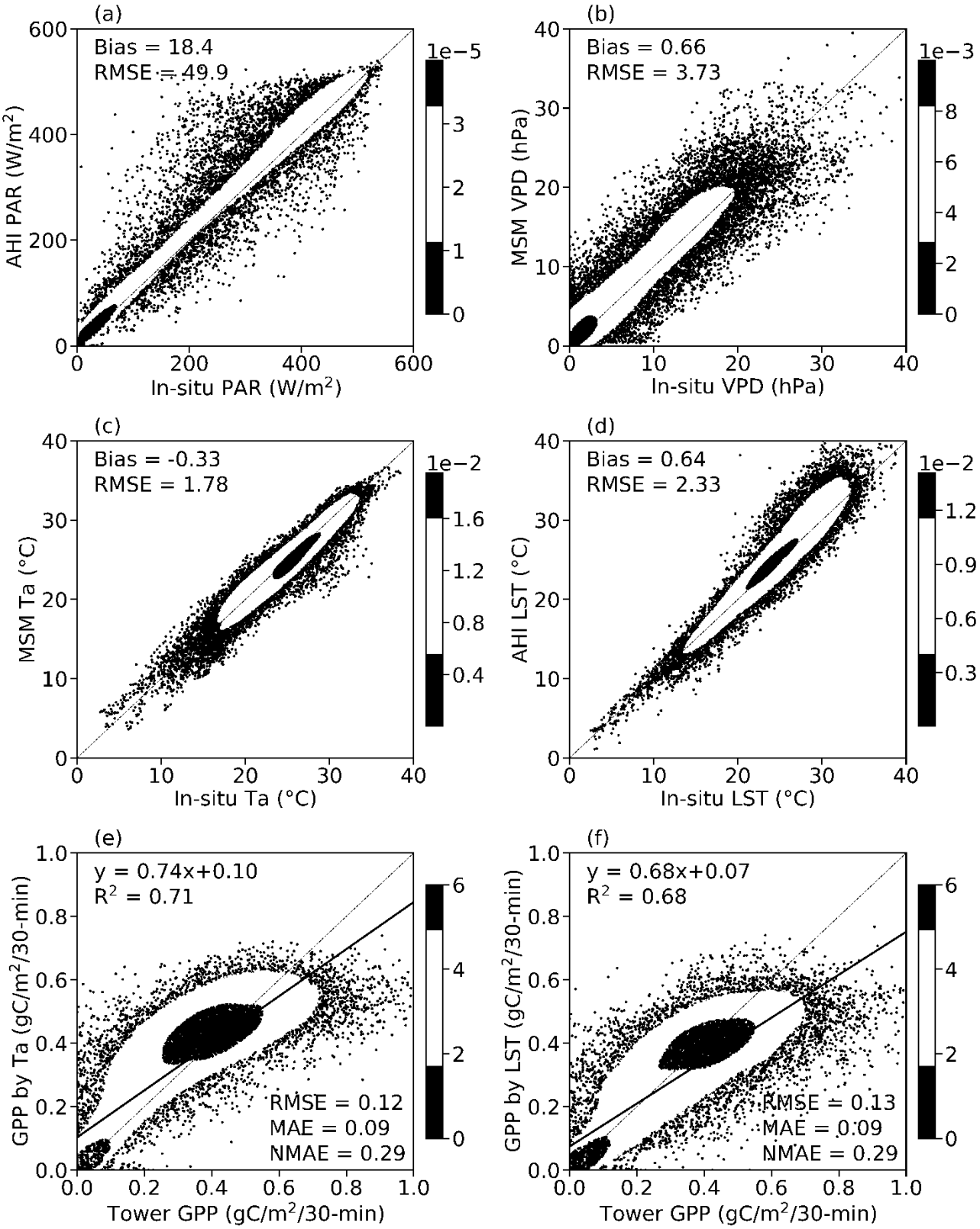

Figure 4. MSM or AHI estimates versus observations at all four sites under clear-sky conditions: (a) PAR, (b) VPD, (c) T_a, (d) LST, (e) GPP with T_s estimation using MSM T_a, and (f) GPP with T_s estimation using AHI LST. The LRC-ECLUE model were used, and the

model parameters were the calibrated values shown in Table 3. Bias shown in (a)–(d) is the mean error. The color bars are probability densities by kernel density estimation.

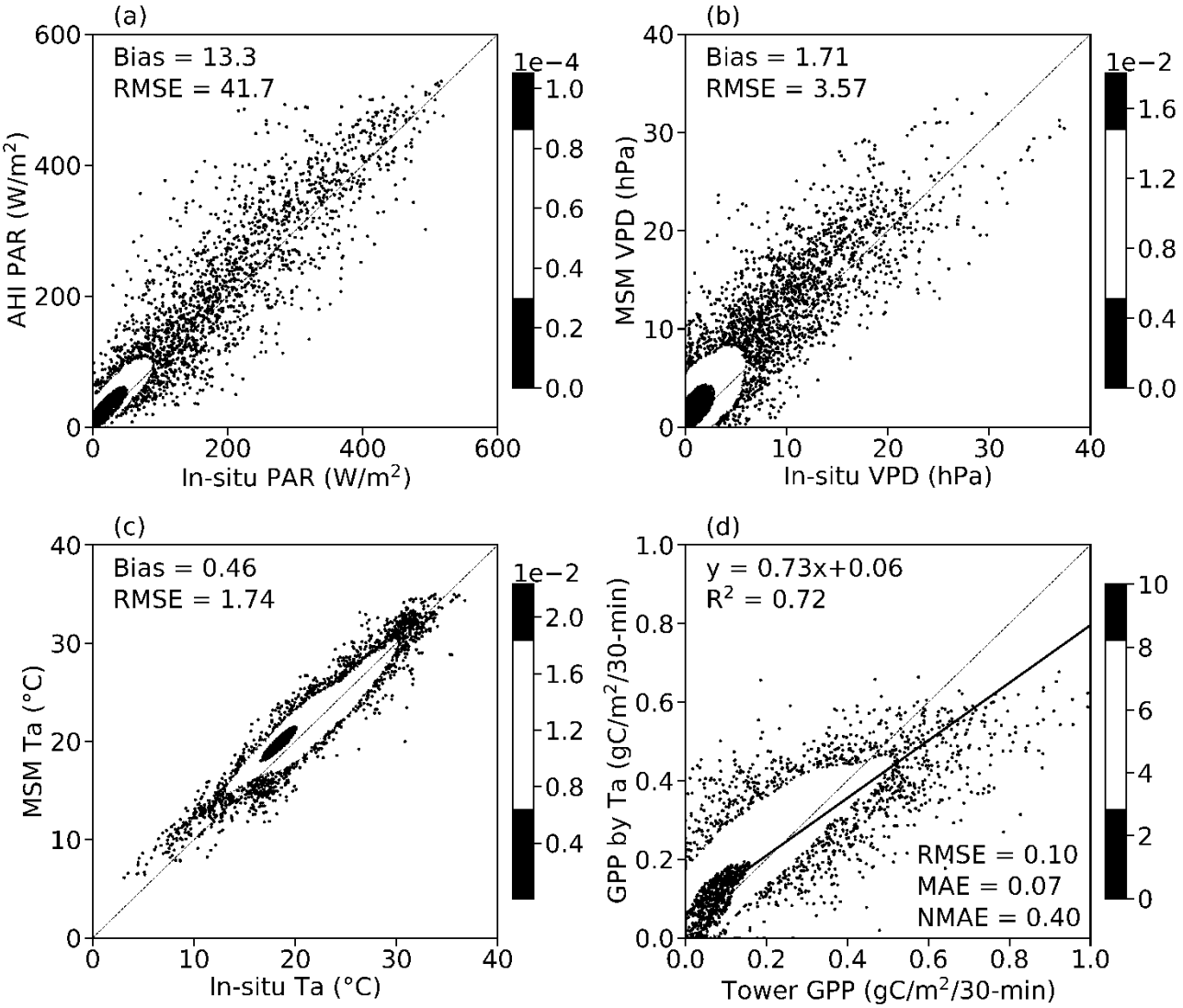

Figure 5. MSM or AHI estimates versus observations at all four sites under cloudy conditions: (a) PAR, (b) VPD, (c) T_a, (d) GPP. The LRC-ECLUE model were used, and the model parameters were the calibrated values shown in Table 3. Bias shown in (a)–(c) is the mean error. The color bars are probability densities by kernel density estimation.

Table 4. Calibrated LRC-ECLUE model parameters when using LST instead of T_a in T_s estimation. The calibration was performed by flux tower observation data.

LUE model	Parameter	GCK	GDK	CRK	TKY
LRC-ECLUE	T_{opt} (℃)	13.7	13.6	36.9	28.9
	VPD_0 (hPa)	23.4	26.1	36.4	39.2
	LUE_{max} (gC·MJ^{-1})	8.95	8.11	8.06	4.43
	α	0.44	0.51	0.51	1.15

β	91.2	82.9	95.2	85.3

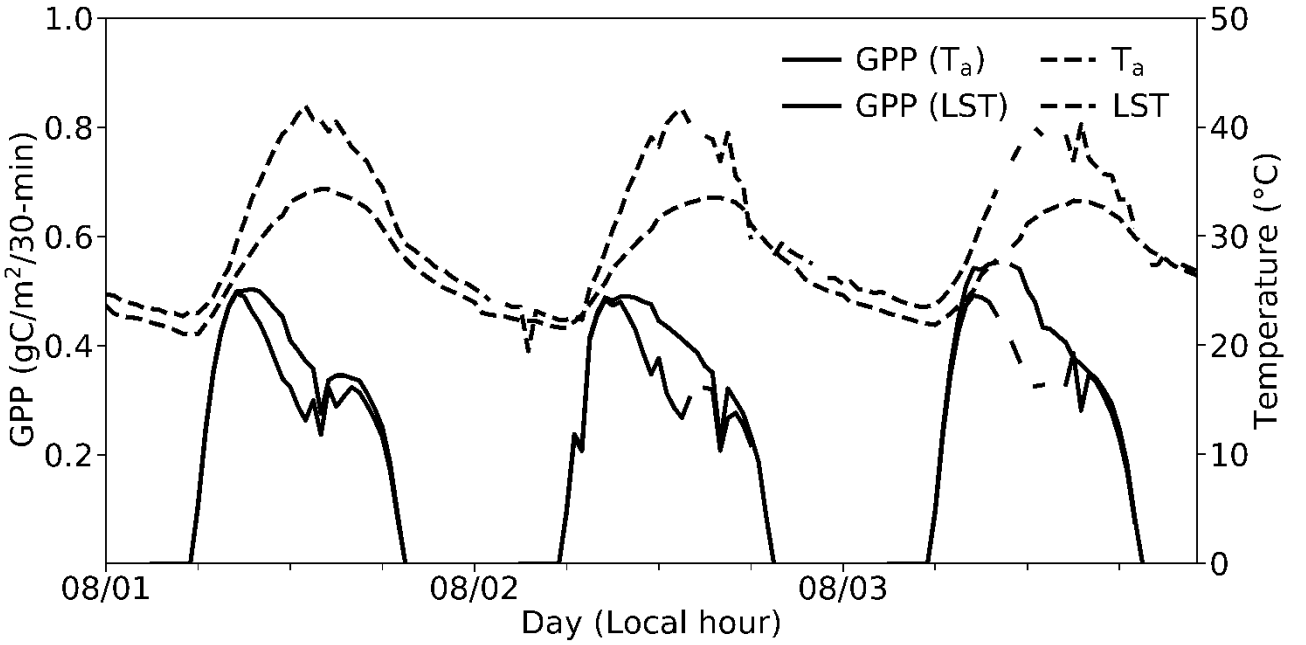

Figure 6. Temporal changes in estimated GPP for a mixed forest pixel located at 37.36 °N–37.38 °N, 128.42 °E–128.44 °E in South Korea during an extreme heatwave (from August 1 to August 3 in 2018). Blue and red solid lines show estimated GPP using MSM T_a and GPP using AHI LST, respectively. Blue and red dashed lines show MSM Ta and AHI LST, respectively.

4. Discussion

4.1. Challenges in estimating diurnal GPP using original LUE models

Both MODIS GPP and EC-LUE models calibrated for diurnal GPP estimation showed R^2 comparable to those for estimation larger than daily scale (Yuan et al., 2014; Jiang et al., 2021; Wang et al., 2021). The differences in calibrated parameters between biome types (Table 3) were larger compared to those of the default values (Running et al., 2000; Mu et al., 2007; Yuan et al., 2014; Yuan et al., 2019). For the MODIS GPP model, both T_{min} and T_{max} in Eq. 3 were originally defined as the daily minimum T_a (Running et al., 2000), but it was found that they can also be used as the maximum and minimum T_a at which photosynthesis is stopped in the diurnal cycle (Khan et al., 2022). The model parameters between the GCK and TKY sites differed substantially, even though both sites were covered by the mixed forests, could be due to the difference in canopy structures (e.g., density, height, tree species and soil types), climate, and elevation (Table 1). Calibration using more sites' data would be needed to obtain parameters representative of each biome type.

The original LUE models were found to have three major problems in diurnal GPP estimation: overestimation around noon and underestimation at evening during extremely hot days, and underestimation under cloudy conditions (Figures 2 and 3). The tendencies of overestimation at high GPP and underestimation at low GPP in the original LUE models shown in Figure 1a–h have been reported in previous studies, both at the diurnal scale (Khan et al., 2022) and daily scale (He et al., 2013; Wang et al., 2021). The underestimation under cloudy conditions would be due to not considering the difference in LUE between direct and diffuse PAR. The LUE of vegetation canopy is enhanced for diffuse PAR than for direct PAR (Alton et al., 2007; Mercado et al., 2009; Zhang et al., 2020). Therefore, the original LUE models were optimized for LUE under clear sky conditions, causing underestimation under cloudy conditions. This study clarified the time of day and observation conditions at which the bias of the original LUE models occur.

4.2. Features of the refined LUE models

By controlling APAR with LRC, it was shown that all the major problems of the original LUE models can be minimized. $APAR_{LRC}$ suppresses extremely high APAR and enhances low APAR (Eq. 8). This reduces the overestimation of GPP during extremely hot days and the underestimation of GPP at twilight and under cloudy conditions (Figures 2 and 3). The effect of suppressing extremely high APAR also contributes to the increase in LUE_{max} and f (Eq. 1). This might have suppressed the overestimation of environmental stress (i.e., underestimation of f) at high T_a and VPD in the afternoon. Another finding is that on extremely hot days, the peaks in the diurnal GPP estimated by LRC models were earlier than those by original models (Figure 3). It might be due to the earlier peak in the diurnal $APAR_{LRC}$ than the diurnal APAR. This feature of the LRC models would also be useful for the shift of the peak to the morning on an extremely hot day in semi-arid regions (Khan et al., 2022).

The improvements in the LUE model by LRC were also favorable in terms of the diurnal variation of FPAR and the impact of diffuse radiation on LUE. The FPAR of the entire vegetation canopy is expected to vary depending on the incident angle of solar radiation (Thomas et al., 2006; Fan et al., 2014). In other words, the FPAR is higher at twilight when the incident angle to the canopy is higher (Li et al., 2015; Liu et al., 2017), because the transmission distance into the canopy is longer. Besides, LUE is enhanced under cloudy conditions and at twilight with longer optical path lengths because the diffuse fraction of PAR is higher (Alton et al., 2007; Mercado et al., 2009; Zhang et al., 2020). These FPAR and LUE variations, which were ignored in the original LUE models, might have resulted in the underestimation at twilight and cloudy conditions (Figures 2 and 3). Thus, considering the diurnal variation of FPAR and the direct and diffuse components of LUE (Yang et al., 2019;

Li et al., 2021b) could improve the original LUE models. However, there is a concern that considering all these factors would complicate the LUE models, which have the advantage of simplicity. Adding LRC term can improve estimation accuracy maintaining the simplicity of the LUE model.

4.3. Uncertainty in regional estimation

The effect of input data uncertainty on regional GPP estimation is greater under cloudy conditions than under clear-sky conditions, as shown by the difference in NMAEs in Figures 4 and 5. An AHI pixel with cloud contamination increases the uncertainty in the direct and diffuse SR_d estimation (Damiani et al., 2018). This uncertainty would be the main error source of GPP estimation under cloudy conditions. Besides, numerical model data covering greater than the regional scale generally have coarser spatiotemporal resolution than AHI observations, and also have difficulty simulating clouds smaller than a few km scale (Saito et al., 2006). Considering sudden changes in T_a/VPD due to short-term rainfall smaller than the mesoscale is important for diurnal GPP estimation, but difficult even using the numerical model data.

When expanding GPP estimation using the LUE model to AHI full disk, it is currently adequate to use of global model data with > 20 km grids and several hourly intervals, such as ECMWF Re-Analysis (ERA5), the Japanese 55-year Reanalysis (JRA-55), and Modern Era Retrospective-Analysis for Research and Applications Version 2 (MERRA-2), not regional/mesoscale model data. However, phenomena showing signals with sub-daily scales are often affected by environmental factors with smaller spatial scales (e.g., midday depression of photosynthesis in agricultural crops: Paul-Limoges et al., 2018). Practical monitoring of environmental stresses in diurnal photosynthesis across the AHI full disk will require spatial downscaling of current numerical model data (Park et al., 2021; Yoo et al., 2022) or alternatively use of satellite products, such as LST. The recently proposed NIRvP-based estimation does not have a capability to incorporate the effects of diurnal stress into GPP estimation (Khan et al., 2022; Jeong et al., 2023). Therefore, input data with high spatiotemporal resolution provide more benefit to the LUE model.

4.4. Applicability of AHI LST

One approach to detect environmental stress at high spatiotemporal resolution is the use of AHI LST. This study demonstrated that AHI LST can be used as a proxy in the LUE model (Figure 5). AHI LST data have a much higher spatiotemporal resolution than numerical model T_a data, thus reflecting the local heating/cooling near the vegetation. Also, LST is a different physical quantity to T_a. The AHI LST is the skin temperature over the top of the

vegetation canopy, whereas the model T_a is the temperature at an uncertain height above the ground. In densely vegetated areas, the LST is closer to the thermal environment experienced by the foliage surface compared to the T_a (Farella et al., 2022), thereby expected to detect environmental stress more accurately. Since this study focused on densely vegetated areas, further investigation regarding the application of LSTs in croplands and semi-arid areas is necessary. Croplands and semi-arid areas are a mixture of bare soil and vegetation. Thus, AHI LST can reach > 60 °C by reflecting bare soil surface on summer clear-sky days, resulting in temperatures quite different from those of vegetated surfaces. When applying LST in agricultural or semi-arid areas, it may be necessary to separate the heat source between vegetation and soil (Kustas et al., 2004) or to do some scaling. LST-based GPP has the disadvantage that it cannot be applied under cloudy conditions due to the limitation on the LST retrieval (Figure 7). To solve this, an all-sky LST (Jia et al., 2022) will be needed in the future. Alternatively, it might be possible to replace LST only for clear sky conditions, because LST-based GPP and T_a-based GPP have almost the identical values except around noon (Figures 4 and 6). Indeed, the estimation of environmental stress is more demanded under clear-sky conditions, which brings hot and dry conditions, rather than under cloudy conditions.

5. Conclusion

The study aims to clarify the applicability of LUE models to the diurnal scale. Using 30-min eddy-covariance observations from four vegetation sites in East Asia, the MODIS and EC-LUE models, and their refined LUE models (LRC-MODIS and LRC-ECLUE models) were calibrated and verified. The results showed that the refined LUE models had higher accuracy than original LUE models. The original LUE models exhibited error characteristics of overestimation around noon and underestimation in the evening on extremely hot days, and underestimation under cloudy conditions. These error characteristics can be partially explained by ignoring the photochemical efficiency of photosynthesis at low irradiance and light saturation at high irradiance. Other possible improvements include considering effects of diurnal variations in FPAR and the direct/diffuse components of LUE. Our refined LUE models can minimize the major errors while maintaining simplicity without incorporating those effects in a precise manner. This study also attempted to apply LRC-ECLUE model using AHI SR_d and MSM T_a and VPD as the primary driving sources. The overall accuracy was comparable to the verification results using site observation data, however, the estimation uncertainty of SR_d under cloudy or cloud mixed scenes was found to be the largest error source. Spatiotemporal resolution of global climate model data is an issue for estimating regional and diurnal environmental stress, thus we attempted to utilize AHI LST as one potential solution. The results showed that LST-based GPP can reflect the extreme

high temperatures near the leaf surface as environmental stress in densely vegetated areas, without degrading the overall estimation accuracy.

Acknowledgments

Himawari-8 gridded data are distributed by the Center for Environmental Remote Sensing (CEReS), Chiba University, Japan. We would like to thank AsiaFlux for providing the following data: Takayama, Cheorwon Rice paddy, Gwangneung Coniferous forest, and Gwangneung Deciduous forest.

Funding

This research received no funding.

References

Allen, R.G., Pereira, L.S., Raes, D., Smith, M., 2006. FAO Irrigation and Drainage Paper No. 56, Crop Evapotranspiration. https://doi.org/10.3390/agronomy9100614

Alton, P.B., North, P.R., Los, S.O., 2007. The impact of diffuse sunlight on canopy light-use efficiency , gross photosynthetic product and net ecosystem exchange in three forest biomes. Glob. Chang. Biol. 13, 776–787. https://doi.org/10.1111/j.1365-2486.2007.01316.x

Beer, C., Reichstein, M., Tomelleri, E., Ciais, P., Jung, M., Carvalhais, N., Rödenbeck, C., Arain, M.A., Baldocchi, D., Bonan, G.B., Bondeau, A., Cescatti, A., Lasslop, G., Lindroth, A., Lomas, M., Luyssaert, S., Margolis, H., Oleson, K.W., Roupsard, O., Veenendaal, E., Viovy, N., Williams, C., Woodward, F.I., Papale, D., 2010. Terrestrial Gross Carbon Dioxide Uptake: Global Distribution and Covariation with Climate. Science (80-.). 329, 834–838. https://doi.org/10.1126/science.1184984

Bessho, K., Date, K., Hayashi, M., Ikeda, A., Imai, T., Inoue, H., Kumagai, Y., Miyasaka, T., Murata, H., Ohno, T., Okuyama, A., Oyama, R., Sasaki, Y., Shimazu, Y., Shimoji, K., Sumida, Y., Suzuki, M., Taniguchi, H., Tsuchiyama, H., Uesaka, D., Yokota, H., Yoshida, R., 2016. An introduction to Himawari-8/9 — Japan's new-generation geostationary meteorological satellites. J. Meteorol. Soc. Japan. Ser. II 94, 151–183. https://doi.org/10.2151/jmsj.2016-009

Boland, J., Ridley, B., Brown, B., 2008. Models of diffuse solar radiation. Renew. Energy 33, 575–584. https://doi.org/10.1016/j.renene.2007.04.012

Cai, W., Prentice, I.C., 2019. Recent trends in gross primary production and their drivers: Analysis and modelling at flux-site and global scales. Environ. Res. Lett. 15. https://doi.org/10.1088/1748-9326/abc64e

Chen, J., Shen, M., Kato, T., 2009. Diurnal and seasonal variations in light-use efficiency in an alpine meadow ecosystem: Causes and implications for remote sensing. J. Plant Ecol. 2,

173–185. https://doi.org/10.1093/jpe/rtp020

Chen, W., Pinker, R.T., Ma, Y., Hulley, G., Borbas, E., Islam, T., Cawse-Nicholson, K.A., Hook, S., Hain, C., Basara, J., 2021. Land surface temperature from GOES-East and GOES-West. J. Atmos. Ocean. Technol. 38, 843–858. https://doi.org/10.1175/JTECH-D-20-0086.1

Chen, W., Zhu, D., Huang, C., Ciais, P., Yao, Y., Friedlingstein, P., Sitch, S., Haverd, V., Jain, A.K., Kato, E., Kautz, M., Lienert, S., Lombardozzi, D., Poulter, B., Tian, H., Vuichard, N., Walker, A.P., Zeng, N., 2019. Negative extreme events in gross primary productivity and their drivers in China during the past three decades. Agric. For. Meteorol. 275, 47–58. https://doi.org/10.1016/j.agrformet.2019.05.002

Cheng, J., Liang, S., Yao, Y., Zhang, X., 2013. Estimating the Optimal Broadband Emissivity Spectral Range for Calculating Surface Longwave Net Radiation. IEEE Geosci. Remote Sens. Lett. 10, 401–405.

Cheng, P., Pour-Biazar, A., McNider, R.T., Mecikalski, J.R., 2020. Validation of GOES-Based Surface Insolation Retrievals and Its Utility for Model Evaluation. J. Atmos. Ocean. Technol. 37, 553–571. https://doi.org/10.1175/JTECH-D-19-0058.1

Ciais, P., Reichstein, M., Viovy, N., Granier, A., Ogée, J., Allard, V., Aubinet, M., Buchmann, N., Bernhofer, C., Carrara, A., Chevallier, F., De Noblet, N., Friend, A.D., Friedlingstein, P., Grünwald, T., Heinesch, B., Keronen, P., Knohl, A., Krinner, G., Loustau, D., Manca, G., Matteucci, G., Miglietta, F., Ourcival, J.M., Papale, D., Pilegaard, K., Rambal, S., Seufert, G., Soussana, J.F., Sanz, M.J., Schulze, E.D., Vesala, T., Valentini, R., 2005. Europe-wide reduction in primary productivity caused by the heat and drought in 2003. Nature 437, 529–533. https://doi.org/10.1038/nature03972

Cox, P.M., Pearson, D., Booth, B.B., Friedlingstein, P., Huntingford, C., Jones, C.D., Luke, C.M., 2013. Sensitivity of tropical carbon to climate change constrained by carbon dioxide variability. Nature 494, 341–344. https://doi.org/10.1038/nature11882

Duan, S.B., Li, Z.L., Zhao, W., Wu, P., Huang, C., Han, X.J., Gao, M., Leng, P., Shang, G., 2021. Validation of Landsat land surface temperature product in the conterminous United States using in situ measurements from SURFRAD, ARM, and NDBC sites. Int. J. Digit. Earth 14, 640–660. https://doi.org/10.1080/17538947.2020.1862319

Fan, W., Liu, Y., Xu, X., Chen, G., Zhang, B., 2014. A new FAPAR analytical model based on the law of energy conservation: A case study in China. IEEE J. Sel. Top. Appl. Earth Obs. Remote Sens. 7, 3945–3955. https://doi.org/10.1109/JSTARS.2014.2325673

Farella, M.M., Fisher, J.B., Jiao, W., Key, K.B., Barnes, M.L., 2022. Thermal remote sensing for plant ecology from leaf to globe. Jouranl Ecol. 110, 1–19. https://doi.org/10.1111/1365-2745.13957

Friedlingstein, P., Jones, M.W., O'Sullivan, M., Andrew, R.M.., Hauck, J., Peters, G.P., Peters, W., Pongratz, J., Sitch, S., Le Quéré, C., Bakker, D.C.E., Canadell, J.G., Ciais, P., Jackson, R.B., Anthoni, P., Barbero, L., Bastos, A., Bastrikov, V., Becker, M., Bopp, L., Buitenhuis,

E., Chandra, N., Chevallier, F., Chini, L.P., Currie, K.I., Feely, R.A., Gehlen, M., Gilfillan, D., Gkritzalis, T., Goll, D.S., Gruber, N., Gutekunst, S., Harris, I., Haverd, V., Houghton, R.A., Hurtt, G., Ilyina, T., Jain, A.K., Joetzjer, E., Kaplan, J.O., Kato, E., Klein Goldewijk, K., Korsbakken, J.I., Landschützer, P., Lauvset, S.K., Lefèvre, N., Lenton, A., Lienert, S., Lombardozzi, D., Marland, G., McGuire, P.C., Melton, J.R., Metzl, N., Munro, D.R., Nabel, J.E.M.S., Nakaoka, S.-I., Neill, C., Omar, A.M., Ono, T., Peregon, A., Pierrot, D., Poulter, B., Rehder, G., Resplandy, L., Robertson, E., Rödenbeck, C., Séférian, R., Schwinger, J., Smith, N., Tans, P.P., Tian, H., Tilbrook, B., Tubiello, F.N., van der Werf, G.R., Wiltshire, A.J., Zaehle, S., 2019. Global Carbon Budget 2019. Earth Syst. Sci. Data 11, 1783–1838. https://doi.org/10.5194/essd-11-1783-2019

Goetz, S.J., Prince, S.D., Goward, S.N., Thawley, M.M., Small, J., 1999. Satellite remote sensing of primary production: an improved production efficiency modeling approach. Ecol. Modell. 122, 239–255. https://doi.org/10.1016/S0304-3800(99)00140-4

Goetz, S.J., Prince, S.D., Small, J., Gleason, A.C.R., 2000. Interannual variability of global terrestrial primary production: Results of a model driven with satellite observations. J. Geophys. Res. Atmos. 105, 20077–20091. https://doi.org/10.1029/2000JD900274

Gu, L., Fuentes, J.D., Shugart, H.H., Staebler, R.M., Black, T.A., 1999. Responses of net ecosystem exchanges of carbon dioxide to changes in cloudiness: Results from two North American deciduous forests. J. Geophys. Res. 104, 31421–31434.

He, M., Ju, W., Zhou, Y., Chen, J., He, H., Wang, S., Wang, H., Guan, D., Yan, J., Li, Y., Hao, Y., Zhao, F., 2013. Development of a two-leaf light use efficiency model for improving the calculation of terrestrial gross primary productivity. Agric. For. Meteorol. 173, 28–39. https://doi.org/10.1016/j.agrformet.2013.01.003

Heinsch, F.A., Maosheng Zhao, Running, S.W., Kimball, J.S., Nemani, R.R., Davis, K.J., Bolstad, P.V., Cook, B.D., Desai, A.R., Ricciuto, D.M., Law, B.E., Oechel, W.C., Hyojung Kwon, Hongyan Luo, Wofsy, S.C., Dunn, A.L., Munger, J.W., Baldocchi, D.D., Liukang Xu, Hollinger, D.Y., Richardson, A.D., Stoy, P.C., Siqueira, M.B.S., Monson, R.K., Burns, S.P., Flanagan, L.B., 2006. Evaluation of remote sensing based terrestrial productivity from MODIS using regional tower eddy flux network observations. IEEE Trans. Geosci. Remote Sens. 44, 1908–1925. https://doi.org/10.1109/TGRS.2005.853936

Hulley, G.C., Hook, S.J., Abbott, E., Malakar, N., Islam, T., Abrams, M., 2015. The ASTER Global Emissivity Dataset (ASTER GED): Mapping Earth's emissivity at 100 meter spatial scale. Geophys. Res. Lett. 42, 7966–7976. https://doi.org/10.1002/2015GL065564

Imada, Y., Shiogama, H., Takahashi, C., Watanabe, M., Mori, M., Kamae, Y., Maeda, S., 2018. Climate Change Increased the Likelihood of the 2016 Heat Extremes in Asia. Bull. Am. Meteorol. Soc. 99, S97–S101. https://doi.org/10.1175/BAMS-D-17-0109.1

Janzen, H.H., 2004. Carbon cycling in earth systems—a soil science perspective. Agric. Ecosyst. Environ. 104, 399–417. https://doi.org/10.1016/j.agee.2004.01.040

Jia, A., Liang, S., Wang, D., 2022. Generating a 2-km, all-sky, hourly land surface temperature product from Advanced Baseline Imager data. Remote Sens. Environ. 278, 113105. https://doi.org/10.1016/j.rse.2022.113105

Jiang, S., Zhao, L., Liang, C., Cui, N., Gong, D., Wang, Y., Feng, Y., Hu, X., Zou, Q., 2021. Comparison of satellite-based models for estimating gross primary productivity in agroecosystems. Agric. For. Meteorol. 297, 108253. https://doi.org/10.1016/j.agrformet.2020.108253

Jung, M., Reichstein, M., Margolis, H.A., Cescatti, A., Richardson, A.D., Arain, M.A., Arneth, A., Bernhofer, C., Bonal, D., Chen, J., Gianelle, D., Gobron, N., Kiely, G., Kutsch, W., Lasslop, G., Law, B.E., Lindroth, A., Merbold, L., Montagnani, L., Moors, E.J., Papale, D., Sottocornola, M., Vaccari, F., Williams, C., 2011. Global patterns of land-atmosphere fluxes of carbon dioxide, latent heat, and sensible heat derived from eddy covariance, satellite, and meteorological observations. J. Geophys. Res. 116, G00J07. https://doi.org/10.1029/2010JG001566

Kalfas, J.L., Xiao, X., Vanegas, D.X., Verma, S.B., Suyker, A.E., 2011. Modeling gross primary production of irrigated and rain-fed maize using MODIS imagery and CO2 flux tower data. Agric. For. Meteorol. 151, 1514–1528. https://doi.org/10.1016/j.agrformet.2011.06.007

Khan, A.M., Stoy, P.C., Joiner, J., Baldocchi, D., Verfaillie, J., Chen, M., Otkin, J.A., 2022. The diurnal dynamics of Gross Primary Productivity using observations from the Advanced Baseline Imager on the Geostationary Operational Environmental Satellite-R Series at an oak savanna ecosystem. J. Geophys. Res. Biogeosciences. https://doi.org/10.1029/2021jg006701

Kustas, W.P., Li, F., Jackson, T.J., Prueger, J.H., Macpherson, J.I., Wolde, M., 2004. Effects of remote sensing pixel resolution on modeled energy flux variability of croplands in Iowa. Remote Sens. Environ. 92, 535–547. https://doi.org/10.1016/j.rse.2004.02.020

Li, L., Du, Y., Tang, Y., Xin, X., Zhang, H., Wen, J., Liu, Q., 2015. A New Algorithm of the FPAR Product in the Heihe River Basin Considering the Contributions of Direct and Diffuse Solar Radiation Separately. Remote Sens. 7, 6414–6432. https://doi.org/10.3390/rs70506414

Li, Xin, Liang, H., Cheng, W., 2021b. Evaluation and comparison of light use efficiency models for their sensitivity to the diffuse PAR fraction and aerosol loading in China. Int. J. Appl. Earth Obs. Geoinf. 95, 102269. https://doi.org/10.1016/j.jag.2020.102269

Li, Xing, Xiao, J., Fisher, J.B., Baldocchi, D.D., 2021a. ECOSTRESS estimates gross primary production with fine spatial resolution for different times of day from the International Space Station. Remote Sens. Environ. 258, 112360. https://doi.org/10.1016/j.rse.2021.112360

Liu, L., Guan, L., Liu, X., 2017. Directly estimating diurnal changes in GPP for C3 and C4 crops using far-red sun-induced chlorophyll fluorescence. Agric. For. Meteorol. 232, 1–9. https://doi.org/10.1016/j.agrformet.2016.06.014

Malakar, N.K., Hulley, G.C., Hook, S.J., Laraby, K., Cook, M., Schott, J.R., 2018. An operational

land surface temperature product for Landsat thermal data: Methodology and validation. IEEE Trans. Geosci. Remote Sens. 56, 5717–5735. https://doi.org/10.1109/TGRS.2018.2824828

Mccree, K.J., 1981. Photosynthetically Active Radiation in Physiological Plant Ecology I. https://doi.org/10.1007/978-3-642-68090-8_3

Mercado, L.M., Bellouin, N., Sitch, S., Boucher, O., Huntingford, C., Wild, M., Cox, P.M., 2009. Impact of changes in diffuse radiation on the global land carbon sink. Nature 458, 1014–1017. https://doi.org/10.1038/nature07949

Michaelis, L., Menten, M.L., 1913. Die Kinetik der Invertinwirkung. Biochem. Z. 49, 333–369.

Monteith, J.L., 1972. Solar Radiation and Productivity in Tropical Ecosystems. J. Appl. Ecol. 9, 747–766. https://doi.org/10.2307/2401901

Mu, Q., Heinsch, F.A., Zhao, M., Running, S.W., 2007. Development of a global evapotranspiration algorithm based on MODIS and global meteorology data. Remote Sens. Environ. 111, 519–536. https://doi.org/10.1016/j.rse.2006.07.007

Myneni, R.B., Hoffman, S., Knyazikhin, Y., Privette, J.L., Glassy, J., Tian, Y., Wang, Y., Song, X., Zhang, Y., Smith, G.R., Lotsch, A., Friedl, M., Morisette, J.T., Votava, P., Nemani, R.R., Running, S.W., 2002. Global products of vegetation leaf area and fraction absorbed PAR from year one of MODIS data. Remote Sens. Environ. 83, 214–231. https://doi.org/10.1016/S0034-4257(02)00074-3

Ozanne, C.H.P., Anhuf, D., Boulter, S.L., Keller, H., Kitching, R.L., Körner, C., Meinzer, F.C., Mitchell, A.W., Nakashizuka, T., Silva Dias, P.L., Stork, N.E., Wright, S.J., Yoshimura, M., 2003. Biodiversity meets the atmosphere: A global view of forest canopies. Science (80-.). 301, 183–186. https://doi.org/10.1126/science.1084507

Park, H., Lee, J., Yoo, C., Sim, S., Im, J., 2021. Estimation of Spatially Continuous Near-Surface Relative Humidity Over Japan and South Korea. IEEE J. Sel. Top. Appl. Earth Obs. Remote Sens. 14, 8614–8626. https://doi.org/10.1109/JSTARS.2021.3103754

Paul-Limoges, E., Damm, A., Hueni, A., Liebisch, F., Eugster, W., Schaepman, M.E., Buchmann, N., 2018. Effect of environmental conditions on sun-induced fluorescence in a mixed forest and a cropland. Remote Sens. Environ. 219, 310–323. https://doi.org/10.1016/j.rse.2018.10.018

Peng, Y., Kira, O., Nguy-Robertson, A., Suyker, A., Arkebauer, T., Sun, Y., Gitelson, A.A., 2019. Gross primary production estimation in crops using solely remotely sensed data. Agron. J. 111, 2981–2990. https://doi.org/10.2134/agronj2019.05.0332

Reeves, M.C., Zhao, M., Running, S.W., 2005. Usefulness and limits on MODIS GPP for estimating wheat yield. Int. J. Remote Sens. 26, 1403–1421. https://doi.org/10.1080/01431160512331326567

Running, S.W., Nemani, R.R., Heinsch, F.A., Zhao, M., Reeves, M., Hashimoto, H., 2004. A continuous satellite-derived measure of global terrestrial primary production. Bioscience 54,

547–560. https://doi.org/10.1641/0006-3568(2004)054[0547:ACSMOG]2.0.CO;2

Running, S.W., Thornton, P.E., Nemani, R., Glassy, J.M., 2000. Global Terrestrial Gross and Net Primary Productivity from the Earth Observing System, Methods in Ecosystem Science. Springer New York, New York, NY. https://doi.org/10.1007/978-1-4612-1224-9

Sulla-Menashe, D., Gray, J.M., Abercrombie, S.P., Friedl, M.A., 2019. Hierarchical mapping of annual global land cover 2001 to present: The MODIS Collection 6 Land Cover product. Remote Sens. Environ. 222, 183–194. https://doi.org/10.1016/j.rse.2018.12.013

Thomas, V., Finch, D.A., McCaughey, J.H., Noland, T., Rich, L., Treitz, P., 2006. Spatial modelling of the fraction of photosynthetically active radiation absorbed by a boreal mixedwood forest using a lidar-hyperspectral approach. Agric. For. Meteorol. 140, 287–307. https://doi.org/10.1016/j.agrformet.2006.04.008

Wang, W., Liang, S., Meyers, T., 2008. Validating MODIS land surface temperature products using long-term nighttime ground measurements. Remote Sens. Environ. 112, 623–635. https://doi.org/10.1016/j.rse.2007.05.024

Wang, Y., Li, R., Hu, J., Fu, Y., Duan, J., Cheng, Y., 2021. Daily estimation of gross primary production under all sky using a light use efficiency model coupled with satellite passive microwave measurements. Remote Sens. Environ. 267, 112721. https://doi.org/10.1016/j.rse.2021.112721

Xia, J., Niu, S., Ciais, P., Janssens, I.A., Chen, J., Ammann, C., Arain, A., Blanken, P.D., Cescatti, A., Bonal, D., Buchmann, N., Curtis, P.S., Chen, S., Dong, J., Flanagan, L.B., Frankenberg, C., Georgiadis, T., Gough, C.M., Hui, D., Kiely, G., Li, J., Lund, M., Magliulo, V., Marcolla, B., Merbold, L., Montagnani, L., Moors, E.J., Olesen, J.E., Piao, S., Raschi, A., Roupsard, O., Suyker, A.E., Urbaniak, M., Vaccari, F.P., Varlagin, A., Vesala, T., Wilkinson, M., Weng, E., Wohlfahrt, G., Yan, L., Luo, Y., 2015. Joint control of terrestrial gross primary productivity by plant phenology and physiology. Proc. Natl. Acad. Sci. U. S. A. 112, 2788–2793. https://doi.org/10.1073/pnas.1413090112

Xu, H., Xiao, J., Zhang, Z., 2020. Heatwave effects on gross primary production of northern mid-latitude ecosystems. Environ. Res. Lett. 15, 074027. https://doi.org/10.1088/1748-9326/ab8760

Yan, K., Park, T., Yan, G., Chen, C., Yang, B., Liu, Z., Nemani, R.R., Knyazikhin, Y., Myneni, R.B., 2016. Evaluation of MODIS LAI/FPAR product collection 6. Part 1: Consistency and improvements. Remote Sens. 8, 1–16. https://doi.org/10.3390/rs8050359

Yang, X., Li, J., Yu, Q., Ma, Y., Tong, X., Feng, Y., Tong, Y., 2019. Impacts of diffuse radiation fraction on light use efficiency and gross primary production of winter wheat in the North China Plain. Agric. For. Meteorol. 275, 233–242. https://doi.org/10.1016/j.agrformet.2019.05.028

Yoo, C., Im, J., Cho, D., Lee, Y., Bae, D., Sismanidis, P., 2022. Downscaling MODIS nighttime land surface temperatures in urban areas using ASTER thermal data through local linear

forest. Int. J. Appl. Earth Obs. Geoinf. 110, 102827. https://doi.org/10.1016/j.jag.2022.102827

Yuan, W., Cai, W., Xia, J., Chen, J., Liu, S., Dong, W., Merbold, L., Law, B., Arain, A., Beringer, J., Bernhofer, C., Black, A., Blanken, P.D., Cescatti, A., Chen, Y., Francois, L., Gianelle, D., Janssens, I.A., Jung, M., Kato, T., Kiely, G., Liu, D., Marcolla, B., Montagnani, L., Raschi, A., Roupsard, O., Varlagin, A., Wohlfahrt, G., 2014. Global comparison of light use efficiency models for simulating terrestrial vegetation gross primary production based on the LaThuile database. Agric. For. Meteorol. 192–193, 108–120. https://doi.org/10.1016/j.agrformet.2014.03.007

Yuan, W., Liu, S., Yu, G., Bonnefond, J.M., Chen, J., Davis, K., Desai, A.R., Goldstein, A.H., Gianelle, D., Rossi, F., Suyker, A.E., Verma, S.B., 2010. Global estimates of evapotranspiration and gross primary production based on MODIS and global meteorology data. Remote Sens. Environ. 114, 1416–1431. https://doi.org/10.1016/j.rse.2010.01.022

Yuan, W., Liu, S., Zhou, Guangsheng, Zhou, Guoyi, Tieszen, L.L., Baldocchi, D., Bernhofer, C., Gholz, H., Goldstein, A.H., Goulden, M.L., Hollinger, D.Y., Hu, Y., Law, B.E., Stoy, P.C., Vesala, T., Wofsy, S.C., 2007. Deriving a light use efficiency model from eddy covariance flux data for predicting daily gross primary production across biomes. Agric. For. Meteorol. 143, 189–207. https://doi.org/10.1016/j.agrformet.2006.12.001

Zhang, Q., She, D., Zhang, L., Wang, G., Chen, J., Hao, Z., 2022. High Sensitivity of Compound Drought and Heatwave Events to Global Warming in the Future. Earth's Futur. 10, 1–22. https://doi.org/10.1029/2022EF002833

Zhang, Z., Zhang, Yongguang, Zhang, Yao, Chen, J.M., 2020. Correcting Clear-Sky Bias in Gross Primary Production Modeling From Satellite Solar-Induced Chlorophyll Fluorescence Data. J. Geophys. Res. Biogeosciences 125, 1–16. https://doi.org/10.1029/2020JG005822

Zscheischler, J., Reichstein, M., Harmeling, S., Rammig, A., Tomelleri, E., Mahecha, M.D., 2014. Extreme events in gross primary production: A characterization across continents. Biogeosciences 11, 2909–2924. https://doi.org/10.5194/bg-11-2909-2014